Dynamic surface displacement measurement using carrier optical vortex interferometer: A numerical study

Jingtao Dong[1,2,a)], Helia Hooshmand[2], Mingyu Liu[3], Samanta Piano[2,b)]

[1] *Anhui Province Key Laboratory of Measuring Theory and Precision Instrument, School of Instrument Science and Opto-electronic Engineering, Hefei University of Technology, Hefei, Anhui 230009, China*

[2] *Manufacturing Metrology Team, Faculty of Engineering, University of Nottingham, Nottingham NG8 1BB, UK*

[3] *School of Engineering, College of Science, University of Lincoln, Lincoln LN6 7TS, UK*

[a)] *jtdong@hfut.edu.cn*

[b)] *samanta.piano@nottingham.ac.uk*

ABSTRACT: The measurement of dynamic surface displacement is crucial in understanding mechanical and thermophysical dynamics at nanometre to micrometre-scale. Interferometers using optical vortices are gaining attention due to their ability to demodulate fringe patterns with helical phase profiles. In this paper, we propose a novel carrier optical vortex interferometer (COVI) that overcomes the limitations of conventional pixelated morphological operations for demodulating fringe patterns. The COVI introduces a carrier frequency by placing a rotating chopper, a collecting lens and a point photodetector at the exit of the interferometer when there is no surface displacement. When the surface moves, the time-dependent total intensity of the chopped fringe pattern produces a Doppler frequency shift with respect to the carrier frequency. Moreover, a high-order Laguerre-Gaussian (LG) beam exhibiting multiple concentric rings is employed to extend the COVI to the dynamic measurement of non-uniform surface displacement with an axisymmetric profile. In this case, the Doppler frequency shift splits into multiple peaks corresponding to the radii of the rings of the LG beam. Locating the Doppler frequency peaks gives an immediate indication of the surface displacement velocities at those radii. Accordingly, the dynamic surface displacement can be retrieved by integrating the velocities over time. The basic principle and the performance of the COVI are theoretically analysed and numerically demonstrated. In addition, the effect of surface misalignment on the displacement measurement is studied thoroughly and the limitations of the measurable velocity are discussed. Although the proposed approach requires further development to make it more applicable in practice, our study provides a first insight into how to measure a dynamic surface displacement using the COVI.

KEYWORDS: optical vortex interferometer, displacement measurement, carrier frequency, Doppler frequency shift

1. INTRODUCTION

Dynamic surface displacement, which refers to the movement or deformation of the surface of an object or material, at nanometre to micrometre-scale is commonly seen in mechanical and thermophysical dynamics. For instance, linear drives in precision positioning systems usually involve uniform surface displacement at constant or non-constant velocities [1-6]. External force-induced mechanical surface deformation or laser-induced thermoelastic surface deformation involves non-uniform surface displacement with an axisymmetric profile at constant or non-constant velocities [7-12]. Measurement of dynamic surface displacement is crucial to understand the dynamics of these systems. Interferometers employing optical vortices have recently been found promising in measuring surface displacement due to their sub-nanometre resolution [11, 13-20]. In the optical vortex interferometer (OVI), the coaxial coherent superposition of a vortex beam, which has a helical phase profile given by $\exp(i\ell\theta)$, where ℓ is the azimuthal order and θ is the azimuthal angle, with either its conjugate (i.e., the azimuthal order of $-\ell$) or a fundamental Gaussian beam produces a petal-like or spiral fringe pattern, which rotates azimuthally as the phase induced by the surface displacement shifts. The high resolution of the OVI in the displacement measurement results from the high accuracy in phase retrieval, which is determined by the angular resolution in identifying the rotation angle of the fringe pattern. The angular resolution can be guaranteed by the 2π benchmark in the azimuthal direction.

Due to the high angular resolution in identifying the rotation angle of the fringe pattern, pixelated morphological operations on the petal-like or spiral fringe patterns are preferred in the phase retrieval of the OVI. In the scenario of uniform surface displacement measurement, locating the centroids of the petals [18, 21-23] is a common operation for the determination of the rotation angle of the fringe pattern. However, the distortion of the petal's intensity profile and the variations in performance among the centroid locating algorithms make them unreliable and imprecise methods. Image correlation [14, 24] and circular cross-correlation [16] are two methods used to determine the rotation angle by calculating the correlation coefficient, which is given by the ratio between the covariance of two successive fringe patterns and the product of their standard deviations. Correlation methods are immune to statistical noise rather than outliers like sudden vibration and air disturbance. Pixel-based differential method [17] was used to improve the angular resolution by suppressing common-mode noise. Nevertheless, the method is susceptible to practical manipulation because a number of pixel pairs with the intensities being anti-correlated must be selected exactly at the specific angular positions on the fringe pattern. Moiré pointer image [20] was proposed to determine the rotation angle. However, the generation of the Moiré pointer image requires complex algorithms including phase map recovery from multiple phase shifting spiral fringe patterns, Zernike polynomial fitting, moiré fringe pattern reconstruction, and Fourier filtering. Notably, the common basis for those morphological operations relies on the fringe

pattern invariance during rotation due to the uniform phase shift. Besides, the angular resolution is always limited by the pixel resolution in morphological operations.

The scenario of non-uniform surface displacement measurement (see the bottom-left inset in Fig. 1) makes the phase retrieval more complicated as the spiral or petal-like fringes rotate at different angles due to the non-uniform phase shift. One intuitive morphological operation is to extract the contour line of a spiral fringe pattern from the origin to the end to approximate the non-uniform phase profile [25-29]. However, the petal-like fringes rotating at different angles at different radii result in highly twisted and stretched petals [11] (see the bottom-right inset in Fig. 1) which hinder the rotation angle determination via morphological operations. Recently, an OVI based on the linear Doppler effect has been proposed to measure an axisymmetric surface deforming at a constant velocity [30]. However, the work focuses on the experimental observation of the Doppler frequency splitting effect, which is a very limited topic that cannot thoroughly reveal the working principle of the OVI and cannot adapt to the scenarios of dynamic uniform and non-uniform surface displacement measurements simultaneously.

To fill this gap, we propose a carrier optical vortex interferometer (COVI), which deploys a detection assembly consisting of a rotating chopper, a collecting lens, and a point photodetector and uses a high-order Laguerre-Gaussian (LG) mode as the probe beam. On the one hand, the detection assembly overcomes the limitations of pixelated morphological operations by producing a carrier in the absence of the surface displacement and introducing a Doppler frequency shift with respect to the carrier frequency in the presence of the dynamic surface displacement. On the other, if a p-radial order LG beam exhibiting p+1 concentric rings is used to probe the dynamic non-uniform surface displacement with an axisymmetric profile, the Doppler frequency shift will split into p+1 peaks corresponding to the radii of the p+1 rings of the LG beam. Locating those frequency peaks near the carrier frequency indicates the velocities of the surface displacement at those radii. Accordingly, the surface displacement at any time can be retrieved by integrating the velocities over time.

In this paper, we introduce the optical layout of the COVI followed by a rigorous theoretical explanation of the working principles of the carrier and the Doppler frequency shift as well as the Doppler frequency splitting. An extensive numerical study on the signal demodulation is then implemented explicitly for the scenarios of uniform and axisymmetric non-uniform surface displacement measurements. The effect of the surface misalignment including the tilt and the lateral offset on the displacement measurement is investigated thoroughly. The limitation factors of the measurable surface displacement velocity are discussed before the conclusion is made.

2. OPTICAL LAYOUT

The optical layout of the proposed COVI based on a typical Mach-Zehnder interferometer is illustrated in Fig.1. A linearly-polarised He-Ne laser beam with a wavelength of $\lambda = 632.8$ nm is first expanded and then directed to the panel of a spatial light modulator (SLM) by a beam splitter (BS1). To generate a high-order $LG_{\ell, p}$ mode with an azimuthal order of ℓ and a radial order of p, a hologram is created by summing the phases of the desired LG mode and a blazed phase grating [31]. The resulting hologram is written on the SLM panel, as shown in the inset below the SLM in Fig.1. The first-order of the diffracted light is selected as the input of the interferometer using a 4f system consisting of two lenses and an adjustable iris.

The LG beam in the measurement arm of the interferometer that passes through the BS2 and the BS3 is used to probe the surface displacement. The measurement LG beam carrying the phase shift induced by the dynamic surface displacement is combined with another reference LG beam at the BS4. The LG beam experiences an odd number of reflections in one arm and an even number in the other, a petal-like fringe pattern is produced at the exit of the interferometer due to the coaxial superposition of conjugated LG beams (i.e., $LG_{\ell, p}$ and $LG_{-\ell, p}$). A detection assembly consisting of a rotating chopper, a collecting lens and a point photodetector (PD) is placed at one exit of the interferometer. The time-dependent total intensity of the petal-like fringe pattern, when passed through the rotating chopper, is thereby converted to a time-domain signal.

A camera is placed at the other exit of the interferometer. The camera works with an iterative phase retrieval algorithm (e.g., the Gerchberg-Saxton algorithm [32]) to optimise a LG beam with a high-quality intensity profile. Moreover, the camera is used to calibrate the radii of the concentric rings of the LG beam by blocking the reference LG beam. The distance from the camera to the BS4 is the same as the distance from the chopper to the BS4 to ensure that the size of the fringe pattern located at the chopper is the same as the one captured by the camera. The camera can be removed after the intensity profile optimisation and the radius calibration of the LG beam are completed.

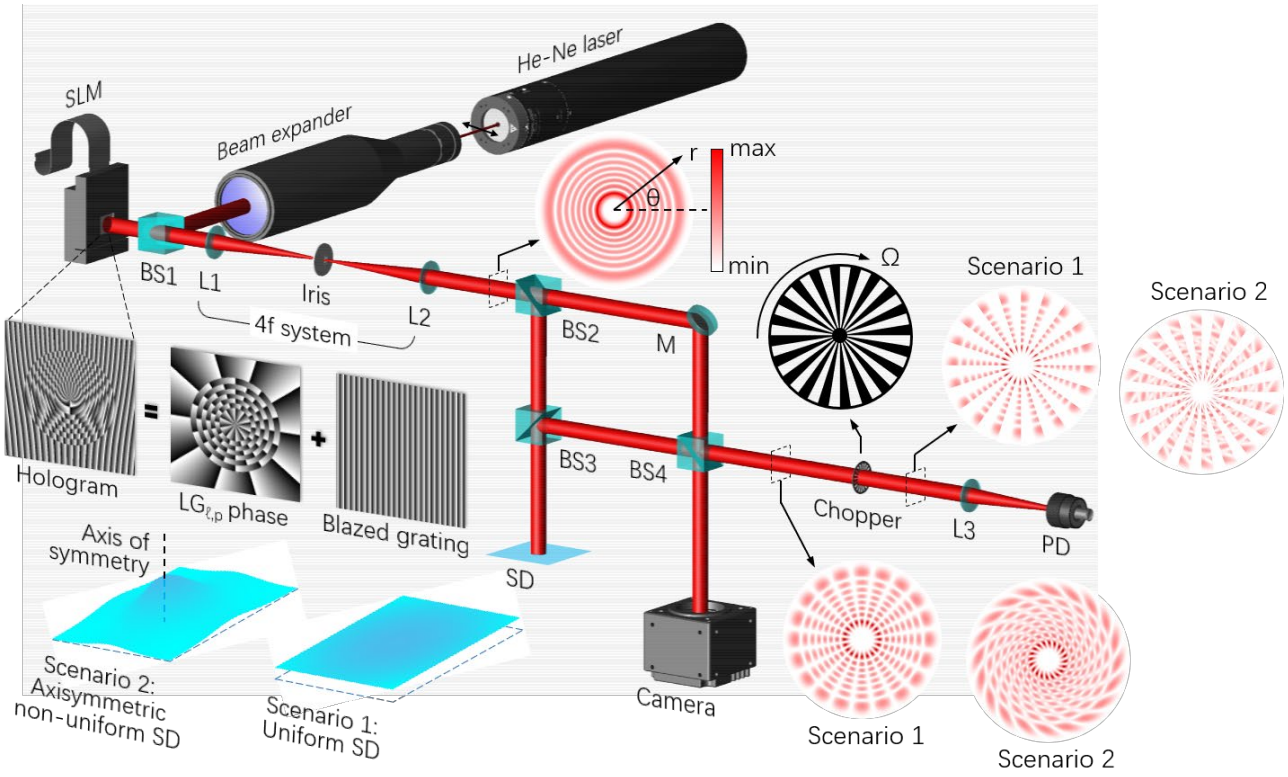

Fig. 1. Optical layout of the carrier optical vortex interferometer (COVI). The inset below the SLM shows the hologram used to generate the LG beam with $\ell = 10$ and $p = 7$. The insets below the hologram illustrate the two scenarios of uniform and axisymmetric non-uniform surface displacement measurements that are studied in this work. The inset above the BS2 shows the intensity distribution of the LG beam after the phase modulation of the SLM. The lower-right insets show the petal-like fringe patterns at the exit of the COVI for the two scenarios. The inset above the chopper illustrates the intensity transmittance function of the chopper, where white is 1 and black representing the chopper blades is 0. The upper-right insets show the fringe patterns when passed through the chopper for the two scenarios. The camera is used for intensity profile optimisation and radius calibration of the LG beam and can be removed later. SLM: spatial light modulator, BS: beam splitter, L: lens, M: mirror, PD: photodetector, SD: surface displacement.

3. WORKING PRINCIPLE

The electric fields of the measurement and reference LG beams in the COVI are expressed as

$$E^{a}_{-\ell,p}(r,\theta) = A^{a}_{-\ell,p}(r)\cdot\exp\left[-i\left(-\ell\theta+\frac{kr^2}{2R}+\varphi_G+\varphi_{SD}\right)\right], \tag{1}$$

$$E^{b}_{\ell,p}(r,\theta) = A^{b}_{\ell,p}(r)\cdot\exp\left[-i\left(\ell\theta+\frac{kr^2}{2R}+\varphi_G\right)\right], \tag{2}$$

with the amplitudes being

$$A^{a}_{-\ell,p}(r)=A^{b}_{\ell,p}(r)=A_{\ell,p}(r)=\sqrt{\frac{2p!}{\pi(p+|l|)!}}\frac{1}{w}\left(\frac{r\sqrt{2}}{w}\right)^{|\ell|}\exp\left(-\frac{r^2}{w^2}\right)L_p^{|\ell|}\left(\frac{2r^2}{w^2}\right), \tag{3}$$

where the superscripts a and b represent the measurement and reference LG beams, respectively; r, θ, and z are the parameters of cylindrical coordinates; k is the wavenumber; the $1/e$ radius of the Gaussian term is given by $w = w_0[(z^2+z_R^2)/z_R^2]^{1/2}$ with w_0 being the beam waist and z_R the Rayleigh range; $L_p^{|\ell|}(x)$ is an associated Laguerre polynomial; $R = z[1+(z_R/z)^2]$ is the radius of curvature of the wavefront at the distance z from the waist; $\varphi_G = (2p+|\ell|+1)\tan^{-1}(z/z_R)$ is the Gouy phase; φ_{SD} is the phase shift induced by the dynamic surface displacement. A LG mode with $p > 0$ comprises p+1 concentric rings with a zero on-axis intensity, as shown in the inset above the BS2 in Fig.1 (e.g., $\ell = 10$ and $p = 7$).

The coaxial superposition of the measurement and reference LG beams produces a petal-like fringe pattern at the exit of the interferometer with the light intensity described as

$$I(r,\theta)=\left(E^{a}_{-\ell,p}+E^{b}_{\ell,p}\right)\left(E^{a}_{-\ell,p}+E^{b}_{\ell,p}\right)^{*}=2\left|A_{\ell,p}(r)\right|^2\cdot\left[1+\cos\left(2\ell\theta-\varphi_{SD}\right)\right], \tag{4}$$

where the phase difference, satisfying $2\ell\theta - \varphi_{SD} = 2\pi n$ (n = 0, 1, 2, …), gives 2ℓ bright petals in the azimuthal direction. The petal-like fringe pattern is modulated by a rotating chopper with a transmittance function $T(\theta, t)$ given by

$$T(\theta,t)=\begin{cases}1, & 2n\dfrac{\pi}{\ell}+\Omega t\le\theta\le(2n+1)\dfrac{\pi}{\ell}+\Omega t\\ 0, & \text{others}\end{cases},\ (n=0,1,...,\ell-1) \tag{5}$$

where Ω (rad/s) is the angular velocity of the chopper and the number of the chopper blades is 2ℓ. Eq.(5) indicates that $T(\theta, t)$ is a square wave with a period of π/ℓ cyclically shifted at an angular frequency of $2\ell\Omega$ in a window of $[0, 2\pi]$. The fringe pattern after being modulated by $T(\theta, t)$ is then collected by lens L3. The total light intensity as a function of time is then expressed by

$$I(t)=\int_0^{2\pi}\int_0^{\infty}T(\theta,t)\cdot I(r,\theta)\,\mathrm{d}r\mathrm{d}\theta=2\int_0^{2\pi}\int_0^{\infty}T(\theta,t)\cdot\left|A_{\ell,p}(r)\right|^2\left[1+\cos\left(2\ell\theta-\varphi_{SD}\right)\right]\mathrm{d}r\mathrm{d}\theta. \tag{6}$$

The frequency spectrum of the time-domain signal $I(t)$ can be analysed following two scenarios.

Scenario 1: It is assumed that the surface displacement has a uniform profile and moves at a velocity v_0. Thus, the phase shift is given by $\varphi_{SD} = (4\pi/\lambda)v_0t$. After substituting φ_{SD} into Eq. (6), we have

$$I(t)=2\int_0^{\infty}\left|A_{\ell,p}(r)\right|^2\mathrm{d}r\cdot\int_0^{2\pi}T(\theta,t)\cdot\left[1+\cos\left(2\ell\theta-4\pi v_0t/\lambda\right)\right]\mathrm{d}\theta. \tag{7}$$

The first integral term on the radius r is time-independent and results in a constant, while the second one on the azimuthal angle θ is time-dependent. Therefore, the frequency component of $I(t)$ can be obtained from the Fourier transform of the time-dependent term

$$\begin{aligned} H(\omega) &\propto \mathcal{F}\left\{\int_0^{2\pi} T(\theta,t)\cdot\left[1+\cos\left(2\ell\theta-4\pi v_0 t/\lambda\right)\right]\mathrm{d}\theta\right\} \\ &= \mathcal{F}\left\{\left[1+\cos\left(2\ell\theta-4\pi v_0 t/\lambda\right)\right]\cdot\int_0^{2\pi} T(\theta,t)\,\mathrm{d}\theta-\int_0^{2\pi}\left[-2\ell\sin\left(2\ell\theta-4\pi v_0 t/\lambda\right)\right]\left[\int_0^{2\pi} T(\theta,t)\,\mathrm{d}\theta\right]\mathrm{d}\theta\right\}, \end{aligned} \tag{8}$$

where $\mathcal{F}$ and ω denote the Fourier transform and angular frequency, respectively. The square wave integral term $\int T(\theta,t)\,\mathrm{d}\theta$ is a triangle wave and can be written in the form of the Fourier series, which contains infinity harmonics (i.e., m = 0, 1, 2, …) with an envelope in the form of sinc^2. The fundamental frequency can be located by only using the first harmonic (i.e., m = 0), so Eq. (8) is written as

$$\begin{aligned} H(\omega) &\propto \mathcal{F}\left\{\left[1+\cos\left(2\ell\theta-4\pi v_0 t/\lambda\right)\right]\frac{8}{\pi^2}\sum_{m=0}^{\infty}\frac{(-1)^m}{(2m+1)^2}\sin\left[2\ell\theta+2\ell\Omega(2m+1)t\right]\right|_0^{2\pi} \\ &\quad +\int_0^{2\pi}\left[2\ell\sin\left(2\ell\theta-4\pi v_0 t/\lambda\right)\right]\frac{8}{\pi^2}\sum_{m=0}^{\infty}\frac{(-1)^m}{(2m+1)^2}\sin\left[2\ell\theta+2\ell\Omega(2m+1)t\right]\mathrm{d}\theta\Bigg\} \\ &\approx \frac{8}{\pi^2}\mathcal{F}\left\{\left[1+\cos\left(2\ell\theta-4\pi v_0 t/\lambda\right)\right]\cdot\sin\left(2\ell\theta+2\ell\Omega t\right)+\ell\theta\cos\left(2\ell\Omega t+4\pi v_0 t/\lambda\right)-\frac{1}{4}\sin\left(2\ell\Omega t+4\ell\theta-4\pi v_0 t/\lambda\right)\right|_0^{2\pi}\Bigg\} \\ &= \frac{8}{\pi^2}\mathcal{F}\left\{\left[1+\cos\left(4\pi\ell-4\pi v_0 t/\lambda\right)\right]\cdot\sin\left(4\pi\ell+2\ell\Omega t\right)+2\pi\ell\cos\left(2\ell\Omega t+4\pi v_0 t/\lambda\right)-\frac{1}{4}\sin\left(2\ell\Omega t+8\pi\ell-4\pi v_0 t/\lambda\right)\right. \\ &\quad \left.-\left[1+\cos\left(4\pi v_0 t/\lambda\right)\right]\cdot\sin\left(2\ell\Omega t\right)+\frac{1}{4}\sin\left(2\ell\Omega t-4\pi v_0 t/\lambda\right)\right\}, \end{aligned} \tag{9}$$

After performing Fourier transform and disregarding the negative frequency and the DC component, Eq.(9) is simplified as

$$H(\omega) \propto 8\sqrt{\frac{2}{\pi}}\ell\cdot\delta\left(\omega-2\ell\Omega-4\pi v_0/\lambda\right), \tag{10}$$

where δ is the Dirac delta function; $4\pi v_0/\lambda = \mathrm{d}\varphi_{SD}/\mathrm{d}t$ is the angular frequency of the phase shift.

If $v_0 = 0$, i.e., $\varphi_{SD} = (4\pi/\lambda)v_0 t = 0$, Eq. (10) reveals that a fundamental frequency is located at $f_c = \omega/2\pi = \ell\Omega/\pi$, which is produced by chopping the static petal-like fringe pattern. Therefore, the time-domain signal in the absence of the surface displacement and the corresponding fundamental frequency f_c are referred to as the carrier and the carrier frequency, respectively.

If v_0 is constant, i.e., $\varphi_{SD} = (4\pi/\lambda)v_0 t \neq 0$, Eq. (10) shows a Doppler frequency shift to be $f_D = 2v_0/\lambda$ with respect to $f_c = \ell\Omega/\pi$.

If v_0 is non-constant, a time-dependent velocity $v(t)$ is used to replace v_0, i.e., $\varphi_{SD} = (4\pi/\lambda)v(t)t$. The Doppler frequency shift becomes $f_D(t) = 2v(t)/\lambda$, which is time-dependent. For such a non-stationary signal, a time-frequency analysis is required to locate the time-dependent Doppler frequency shift.

We emphasise that if $\Omega = 0$ rad/s, then the carrier frequency is $f_c = \ell\Omega/\pi = 0$ Hz. When the surface is displacing at a velocity of v_0, the frequency will shift to $f_c \pm f_D = |0 \pm 2v_0/\lambda|$ Hz. The absolute sign $|\bullet|$ means that the Fourier transform of the time-domain signal results in positive frequencies only. Therefore, the COVI is lack of distinguishing the direction of surface displacement although it can still obtain the surface displacement velocity.

Scenario 2: It is assumed that the surface displacement has an axisymmetric non-uniform profile, and the surface moves at a velocity $v(r)$. The phase shift is then given by $\varphi_{SD}(r_j) = (4\pi/\lambda)v(r_j)t$ with r_j being the discretised radius sampled by the camera pixel and $j = 0,1,2, \ldots, M$ being the sampling length of the radius. After substituting $\varphi_{SD}(r_j)$ into Eq. (6), we obtain the following equation for the light intensity

$$I(t) = \sum_{j=0}^{M-1} 2\left|A_{\ell,p}\left(r_j\right)\right|^2 \int_0^{2\pi} T(\theta,t)\cdot\left\{1+\cos\left[2\ell\theta - 4\pi v\left(r_j\right)t/\lambda\right]\right\}\mathrm{d}\theta. \tag{11}$$

The Fourier transform of Eq. (11) is then expressed as

$$H(\omega) = \sum_{j=0}^{M-1} 2\left|A_{\ell,p}\left(r_j\right)\right|^2 \mathcal{F}\left[\int_0^{2\pi} T(\theta,t)\cdot\left\{1+\cos\left[2\ell\theta - 4\pi v\left(r_j\right)t/\lambda\right]\right\}\mathrm{d}\theta\right]. \tag{12}$$

The Fourier term in Eq. (12) is now the same as the first line of Eq. (8). After applying the partial integration and the first harmonic approximation to Eq. (12) as did in Eqs. (8) and (9), and further disregarding the negative frequency and the DC component, the frequency spectrum is simplified as

$$H(\omega) \propto 8\sqrt{\frac{2}{\pi}}\ell\cdot\sum_{j=0}^{M-1} 2\left|A_{\ell,p}\left(r_j\right)\right|^2 \cdot\delta\left[\omega - 2\ell\Omega - 4\pi v\left(r_j\right)/\lambda\right]. \tag{13}$$

If $v(r_j)$ is constant at each radius r_j, Eq. (13) reveals a Doppler frequency shift to be $f_D(r_j) = 2v(r_j)/\lambda$ weighted by $16\sqrt{2/\pi}\ell\left|A_{\ell,p}\left(r_j\right)\right|^2$ at each radius r_j. This means that the spectrum distribution given by Eq. (13) looks the same as the intensity profile of the LG beam. Therefore, if the intensity distribution of the LG beam shows p+1 concentric rings, the spectrum will split into p+1 Doppler frequency peaks, which correspond to the radii of the p+1 concentric rings of the LG beam. Notably, although the actual spectrum distribution is slightly different from Eq. (13) as the high-order harmonics in the Fourier transform

of $\int T(\theta,t)\mathrm{d}\theta$ are ignored, the Doppler frequency splitting still holds and the peak frequencies determined by the first harmonic don't change.

If $v(r_j)$ is non-constant at each radius r_j, a time-dependent velocity $v(r_j, t)$ is used to replace $v(r_j)$. The split Doppler frequency peaks become $f_D(r_j, t) = 2v(r_j, t)/\lambda$, which shift as a function of time. Similarly, a time-frequency analysis is needed to locate those time-dependent frequency peaks.

The locations of the Doppler frequency peaks give the velocities of the surface displacement at the corresponding radii. The dynamic surface displacement can be retrieved by integrating the velocities over time.

4. UNIFORM SURFACE DISPLACEMENT

The uniform surface displacement measurement is the most common scenario in linear positioning systems like nano-coordinate measuring machines (nano-CMMs) [4-6]. In the axis measurement of a nano-CMM, the target that the laser beam probes is usually a smooth uniform surface moving at a constant velocity or a time-dependent velocity. In this section, we demonstrate the capabilities of the COVI numerically in the measurement of uniform surface displacement.

4.1. Constant velocity

We first obtained the time-domain light intensity (i.e., the carrier), as shown in Fig. 2(a), using Eq.(6) with $\ell = 10$ and $p = 7$ for the LG mode, $\Omega = \pm 10\pi$ rad/s for the chopping angular frequency, $\varphi_{SD} = 0$ for the phase shift, $F_s = 400$ Hz for the sampling rate, and $N = 4000$ being the sampling length. The intensity variation of the carrier is caused by chopping the static petal-like fringe pattern, as illustrated in the insets of Fig. 2(a). After taking the discrete Fourier transform (DFT) of the carrier, the carrier frequency f_c was retrieved to be 100 Hz, as shown in Fig. 2(b), which matches the theoretical one calculated by $f_c = \ell\Omega/\pi = 100$ Hz. This is because the numerically retrieved f_c falls right into a DFT bin [33] with a width of 0.1 Hz, which is given by the frequency resolution defined by $\Delta f = F_s/N$. Moreover, the carrier frequency is independent of the chopping direction because only the single-sided spectrum (i.e., the positive part) of the DFT algorithm is always taken as the frequency spectrum in practice, i.e., $f_c = |\ell\Omega/\pi|$. Notably, the carrier in Fig. 1(a) is a triangle-like wave and its DFT appears as infinite harmonics with an envelope in the form of sinc^2, which agrees with the mathematical description of Eq. (9).

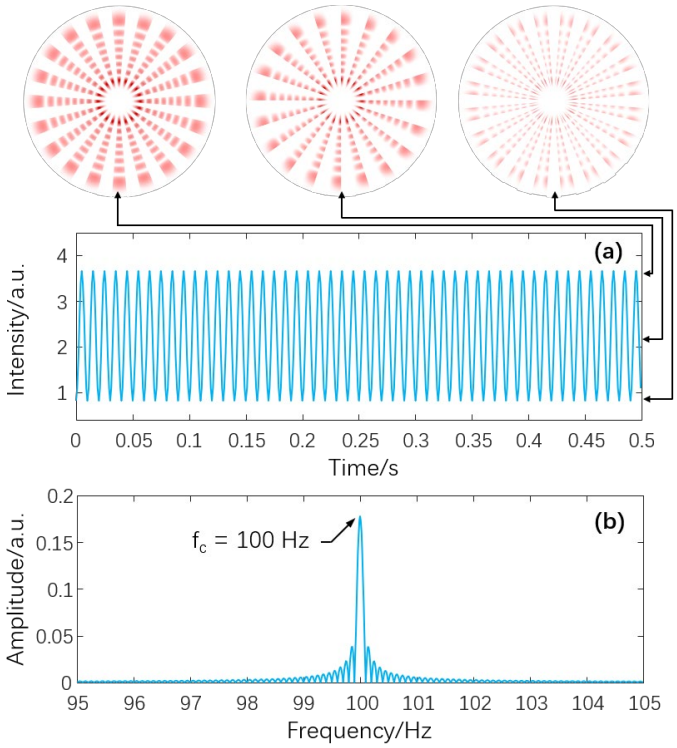

Fig. 2. (a) The carrier obtained in the absence of surface displacement, i.e., the phase shift $\varphi_{SD} = 0$. Only the signal within 0.5 s is displayed for visual clarity. The insets show the chopped fringe patterns corresponding to the maximum, average, and minimum intensities of the carrier. (b) The frequency spectrum of the carrier. Other parameters are $\ell = 10$, $p = 7$, $\Omega = \pm 10\pi$ rad/s, and $F_s = 400$ Hz.

When the uniform surface moves at a constant velocity of $v_0 = 0.5$ μm/s, the time-domain signal for $\Omega = 10\pi$ rad/s varies slowly compared to the carrier because the petal-like fringe pattern and the chopper rotate in the same direction, as shown in the solid blue line in Fig. 3(a). Considering that the DFT bin width is limited to 0.1 Hz at the sampling length of $N = 4000$, we increased the sampling length ten-fold by zero-padding to narrow the DFT bin width down to 0.01 Hz. A negative Doppler frequency shift is therefore obtained to be $f_D = -1.58$ Hz with respect to f_c, as shown in Fig. 3(c). If the chopper and the fringe pattern rotate in an opposite direction, i.e., $\Omega = -10\pi$ rad/s, the time-domain signal varies faster than the carrier, as shown in Fig. 3(b). The DFT of the time-domain signal results in a positive Doppler frequency shift of $f_D = 1.58$ Hz with respect to f_c, as shown in Fig. 3(c), which has a difference of $f_D \approx 2.8\times10^{-4}$ Hz (corresponding to a velocity error of $v_0 = \lambda f_D/2 = 0.088$ nm/s) with respect to the theoretical one that is calculated by $f_D = 2v_0/\lambda$ with $v_0 = 0.5$ μm/s and $\lambda = 632.8$ nm. This frequency difference is reasonable because the numerically retrieved f_D cannot fall right into the DFT bin determined by its theoretical one with many decimals.

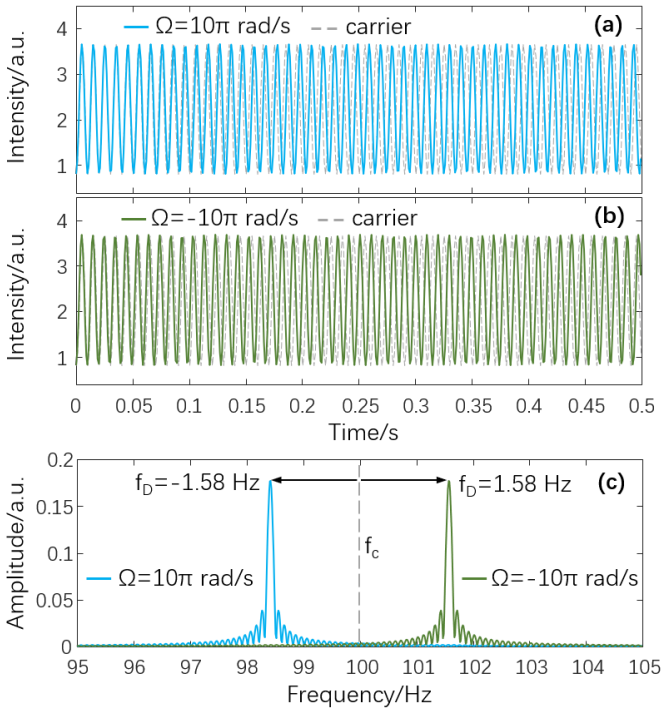

Fig. 3. The time-domain signal for the uniform surface displacement with (a) $v_0 = 0.5$ μm/s and $\Omega = 10\pi$ rad/s (the solid blue line), and (b) $v_0 = 0.5$ μm/s and $\Omega = -10\pi$ rad/s (the solid green line). In (a) and (b), the carrier is displayed in the dashed grey line for comparison, and only the signals within 0.5 s are displayed for visual clarity. (c) The frequency spectra of the time-domain signals in (a) and (b). Other parameters are $\ell = 10$, $p = 7$, and $F_s = 400$ Hz.

4.2. Non-constant velocity

If the uniform surface moves at a time-dependent velocity of $v(t) = a \times t = 5t$ μm/s, where $a = 5$ μm/s^2 is a constant acceleration, the time-domain signals for $\Omega = 10\pi$ rad/s and $\Omega = -10\pi$ rad/s are displayed in Figs. 4(a) and 4(b), respectively. The synchrosqueezed wavelet transform [34] with the Morlet wavelet as the basis function was used to numerically retrieve the time-frequency representations, as shown in the solid lines in Fig. 4(c). The linear up-chirp and down-chirp corresponding to $\Omega = -10\pi$ rad/s and $\Omega = 10\pi$ rad/s, respectively, that start at the carrier frequency of $f_c = 100$ Hz were observed. Similarly, if the surface displacement velocity is $v(t) = a(t) \times t = 2t^2$ μm/s, where $a(t) = 2t$ μm/s^2 is a non-constant acceleration, the time-frequency representations show the quadratic up-chirp and down-chirp for $\Omega = -10\pi$ rad/s and $\Omega = 10\pi$ rad/s, respectively, as shown in the solid lines in Fig. 4(d). The maximum energy time-frequency ridge can be extracted to retrieve the Doppler frequency shifts with respect to f_c at the specific time. The Doppler frequency shifts $f_D(t)$ are then used to obtain the dynamic surface displacement by $u_z\big|_{t=t_0} = \int_0^{t_0} v(t)\,\mathrm{d}t = \int_0^{t_0} \lambda \cdot f_D(t)/2\,\mathrm{d}t$. The theoretical Doppler frequency shifts given by $f_D(t) = 2v(t)/\lambda$ are shown by the dashed lines in Figs. 4(c) and 4(d), which are in good agreement with the ones retrieved numerically.

Note that if only Scenario 1 is of interest, the radial order p of the LG beam can be an arbitrary integer because the petal-like fringes at the different radii rotate at the same velocity as the surface moves uniformly.

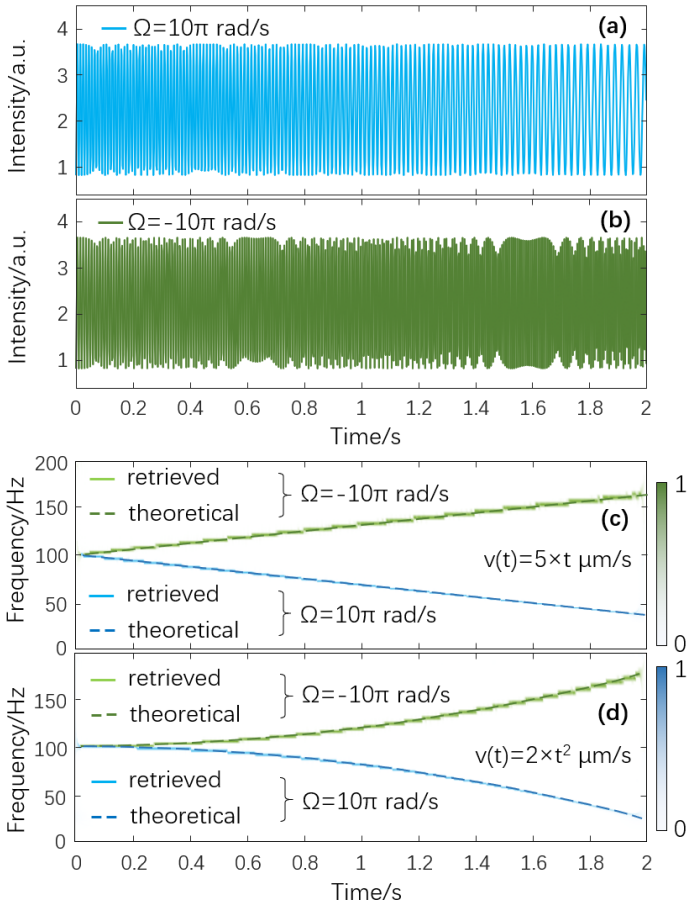

Fig. 4. The time-domain signal for the uniform surface displacement with (a) $v(t) = a{\times}t = 5t$ μm/s and $\Omega = 10\pi$ rad/s, and (b) $v(t) = a{\times}t = 5t$ μm/s and $\Omega = -10\pi$ rad/s. Only the signals within 1 s are displayed for visual clarity in (a) and (b). (c) The time-frequency representations (the solid lines) of the time-domain signals in (a) and (b). (d) The time-frequency representations (the solid lines) of the time-domain signals for the uniform surface displacement with $v(t) = a(t){\times}t = 2t^2$ μm/s and $\Omega = \pm 10\pi$ rad/s. The time-domain signals are not shown here. In (c) and (d), the dashed lines are the theoretical Doppler frequency shifts given by $f_D(t) = 2v(t)/\lambda$; the colorbars on the right indicate the normalized energy of the time-frequency representations. Other parameters are $\ell = 10$, $p = 7$, and $F_s = 400$ Hz.

5. NON-UNIFORM SURFACE DISPLACEMENT

The intensity profile of concentric rings of the LG beam offers a way to measure the axisymmetric non-uniform surface displacement, which is of great interest in studying the mechanical deformation of a surface under external force [10] and the thermoelastic deformation of a surface heated by a Gaussian laser beam [11, 12]. Therefore, we use a surface with a Gaussian distribution to demonstrate how to measure such axisymmetric non-uniform surface displacement using the COVI.

5.1. Constant velocity

Referring to Fig.5, the measurement LG beam with p+1 concentric rings hits an axisymmetric non-uniform surface displacement. A higher radial order LG beam (e.g., p = 10) was used to cover the region of interest of the surface displacement. Thus, the concentric rings at the different radii carry the different phase shifts induced by the different surface displacement velocities. The radii r_n can be found by calculating the power-weighted mean radius of each ring, which is given by

$$r_n = \frac{\sum_{j=0}^{M-1}\left[I\left(r_j\right)\cdot r_j\right]}{\sum_{j=0}^{M-1} I\left(r_j\right)}, \quad n = 1,2,...,p+1 \tag{14}$$

where r_j is the discretised radius of the LG beam; M is the sampling length of the radius; $I(r)$ is the intensity profile of the LG beam with ℓ = 10, p = 10 as a function of radius, as shown by the solid red line in Fig. 5(a). Eq. (14) can be used to calculate the radii of the rings in practice. We emphasise that for a fixed radial order p, one can adjust the waist w_0 of the LG beam in Eq. (3) to alter the radii of the rings for customising the lateral resolution of the surface displacement measurement. The radii r_n obtained using Eq. (14) are indicated by the dashed lines in Fig. 5.

We assumed that the velocity of the axisymmetric non-uniform surface displacement has a Gaussian profile

$$v\left(r\right) = v_0 \cdot \exp\left(r^2/\sigma^2\right), \tag{15}$$

where σ = 3 mm and v_0 = 1 μm/s at r = 0 mm, as shown in Fig. 5(b). With Eq. (15) the theoretical velocities at the radii r_n are given by $v^{thr}(r_n) = v_0 \cdot \exp(r_n^2/\sigma^2)$ and the corresponding theoretical Doppler frequencies are $f_D^{thr}(r_n) = 2v^{thr}(r_n)/\lambda$.

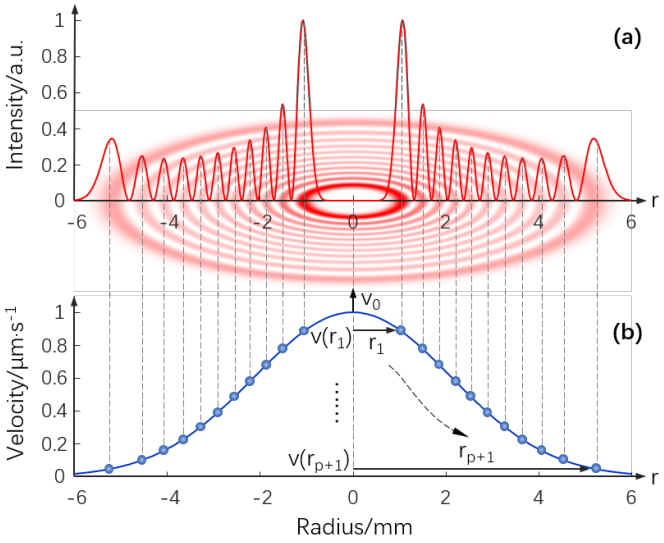

Fig. 5. (a) The intensity pattern and the intensity profile of the LG beam with $\ell = 10$, $p = 10$. The power-weighted mean radii r_n of the rings of the LG beam are indicated by the dashed lines. (b) The velocity profile of the axisymmetric non-uniform surface displacement given by Eq. (15) with $v_0 = 1$ μm/s at $r = 0$ mm. The dots indicate the theoretical velocities at the radii r_n. Notably, if the surface has a tilt angle or a lateral offset, the same radius will possess different velocities.

Figure 6(a) shows the time-domain signal for $v_0 = 1$ μm/s at $r = 0$ mm and $\Omega = -10\pi$ rad/s. The signal envelope varies in an oscillating manner, indicating that the signal is a composition of multiple frequencies. The intensity variation of the signal vanishes after 10 s because the petal-like fringes highly twist and stretch so that the total intensity of the fringe pattern has been changed inconsiderably when passed through the rotating chopper. The insets in Fig. 6(a) show the twisted and stretched fringe patterns before chopping at $t = 1$, 3, 6, and 10 s. An advantage of the proposed COVI is that the conventional morphological operation on the fringe pattern fails after around 3 s due to the largely distorted petals, while the fringe patterns still contribute to the time-domain signal until around 10 s. This means that the dynamic range of the surface displacement measurement using the COVI increases compare to the one using morphological operations.

The frequency spectrum of the time-domain signal indicated by the solid green line in Fig. 6(b) shows that the Doppler frequency shift splits into eleven (i.e., $p+1 = 11$) peaks to the right of the carrier frequency, corresponding to eleven radii of the LG beam given by Eq. (14). The larger the radius, the smaller the surface displacement velocity, and the smaller the Doppler frequency shift. The Doppler peak frequencies with respect to f_c are taken as the ones retrieved numerically, i.e., $f_D^{rtr}(r_n)$, and the retrieved velocities at those radii are obtained by $v^{rtr}(r_n) = f_D^{rtr}(r_n)\lambda/2$. The time-domain signal for $\Omega = 10\pi$ rad/s looks like the one for $\Omega = -10\pi$ rad/s and is not shown here. Its spectrum is shown by the solid blue line in Fig. 6(b), which is the same as the one for $\Omega = -10\pi$ rad/s except that the Doppler frequency peaks are mirrored to the left of the carrier frequency. In what follows, we only investigate signals for $\Omega = -10\pi$ rad/s for convenience.

Figure 6(c) shows the theoretical and retrieved Doppler peak frequencies at the radii r_n, i.e., $f_D^{thr}(r_n)$ and $f_D^{rtr}(r_n)$, which are in good agreement. The frequency differences given by $f_D^{rtr}(r_n) - f_D^{thr}(r_n)$ are within the range of [-0.0277 Hz, 0.0106 Hz], as shown in Fig. 6(d). This difference in frequencies is attributed to two aspects. One aspect is the frequency estimation error due to DFT bin, which has been discussed in Section IV.A. Higher frequency resolution results in a narrower DFT bin, and consequently more accurate frequency estimation. The other one is the discretisation error in the spatial domain. In the numerical study, the light field and the surface displacement are both sampled discretely in the spatial domain (e.g., 512×512 pixels in this work) so that the light intensity and the radius of the LG beam should correspond to pixel indices, which are integers. However, Eq. (14) usually gives pixel indices with decimals, which results in an inevitable discretisation error in the numerical study only. Higher pixel resolution results in smaller discretisation errors, however, with lower computational

efficiency. In practice, the intensity profile of the light field is continuous, so the decimals resulting from Eq. (14) act as sub-pixel interpolation, which makes the radius calculation and the frequency estimation more accurate.

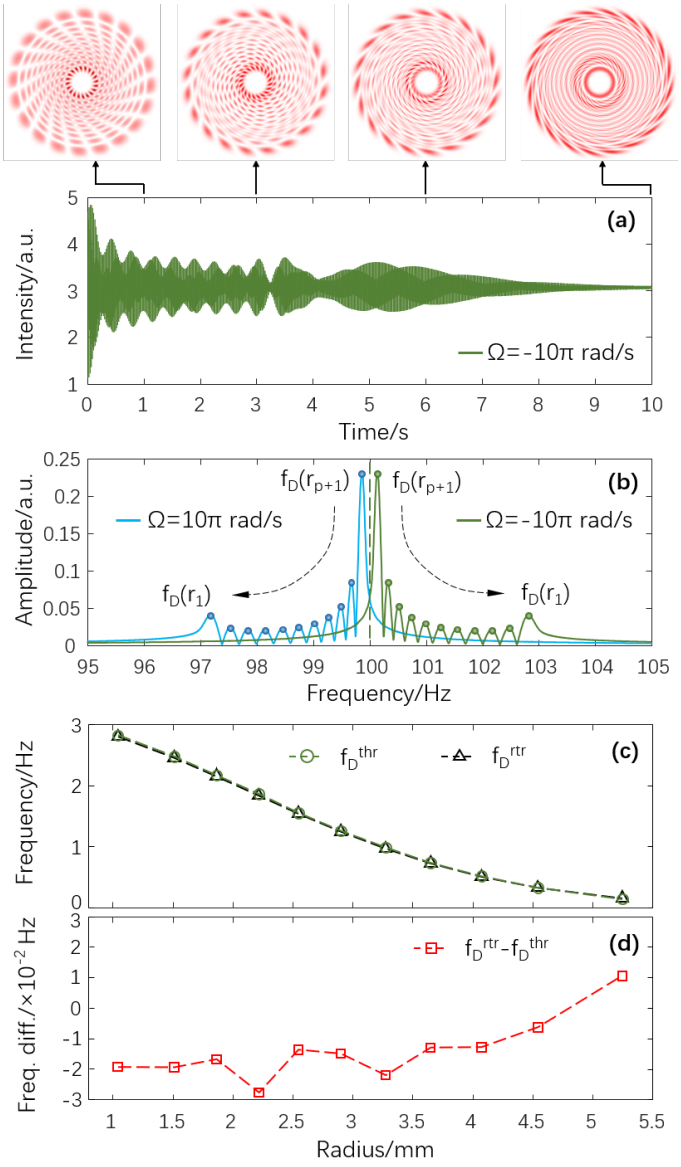

Fig. 6. (a) The time-domain signal for the axisymmetric non-uniform surface displacement with v_0 = 1 μm/s at r = 0 mm and Ω = –10π rad/s. The insets are the fringe patterns before chopping at t = 1, 3, 6, and 10 s. (b) The solid green line is the frequency spectrum of the time-domain signal in (a). The solid blue line is the frequency spectrum for Ω = 10π rad/s. The dashed line at 100 Hz indicates the carrier frequency. (c) The theoretical and retrieved Doppler peak frequencies at the radii r_n and (d) their frequency differences. Other parameters are ℓ = 10, p = 10, and F_s = 250 Hz.

Figure 7(a) displays the spectra of the time-domain signals for v_0 = 0.1 and 0.5 μm/s at r = 0 mm (besides v_0 = 1 μm/s) for comparison. Since lower velocity results in a smaller Doppler frequency shift, the sampling length or the length after zero-

padding should be increased proportionally by two-fold and ten-fold for v_0 = 0.1 and 0.5 μm/s, respectively, compared with that for v_0 = 1 μm/s to alleviate frequency estimation error due to a large DFT bin width. Fig. 7(b) shows the differences between the theoretical and retrieved Doppler peak frequencies at the radii r_n, i.e., $f_D^{rtr}(r_n) - f_D^{thr}(r_n)$, for v_0 = 0.1, 0.5, and 1 μm/s, respectively. The differences between the theoretical and retrieved surface displacement velocities at the radii r_n are indicated by the right vertical axis of Fig. 7(b) since they are directly given by $v^{rtr}(r_n) - v^{thr}(r_n) = [f_D^{rtr}(r_n) - f_D^{thr}(r_n)]\lambda/2$, which are only scaled by a factor of $\lambda/2$. The differences in the Doppler peak frequencies and the surface displacement velocities are on the order of one-hundredth of a Hertz and nanometres per second, respectively. The relative errors of the retrieved Doppler peak frequencies, i.e., $|f_D^{rtr}(r_n) - f_D^{thr}(r_n)|/f_D^{thr}(r_n)$, and those of the retrieved surface displacement velocities, i.e., $|v^{rtr}(r_n) - v^{thr}(r_n)|/v^{thr}(r_n)$, share the same vertical axis in Fig. 7(c). It is shown that the relative errors for the different surface displacement velocities are consistent because we used a narrower DFT bin for a smaller displacement velocity. The relative error is less than ±3% and it is attributed to the discretisation error and the frequency estimation error due to the DFT bin as discussed in the descriptions for Fig. 6(c).

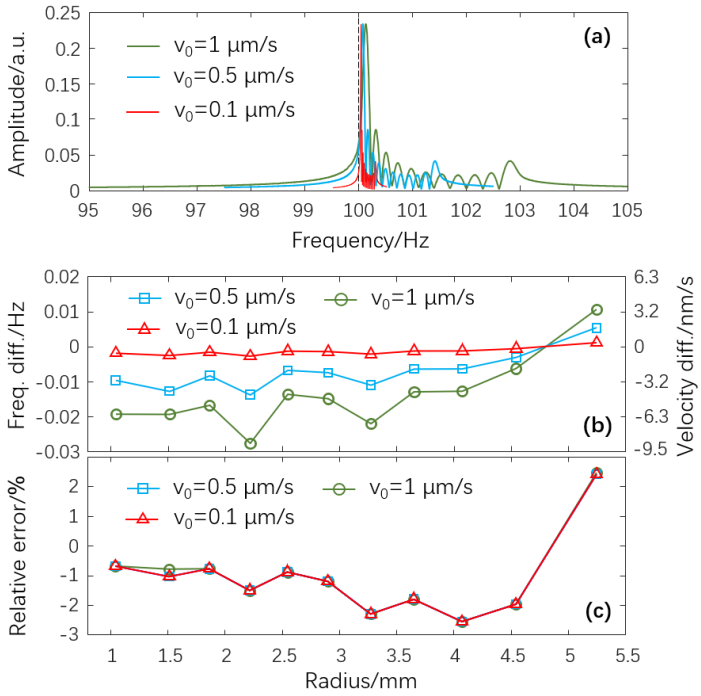

Fig. 7. (a) The spectra of the time-domain signals for the axisymmetric non-uniform surface displacement with v_0 = 0.1, 0.5, and 1 μm/s at r = 0 mm. The dashed line indicates the carrier frequency. (b) The differences between the theoretical and retrieved Doppler peak frequencies at the radii r_n, i.e., $f_D^{rtr}(r_n) - f_D^{thr}(r_n)$, for v_0 = 0.1, 0.5, and 1 μm/s (referring to the left vertical axis) and the corresponding differences between the theoretical and retrieved velocities, i.e., $v^{rtr}(r_n) - v^{thr}(r_n) = [f_D^{rtr}(r_n) - f_D^{thr}(r_n)]\lambda/2$ (referring to the right vertical axis). (c) The relative errors of the retrieved Doppler peak frequencies and the retrieved surface displacement velocities. Other parameters are ℓ = 10, p = 10, and F_s = 250 Hz.

5.2. Non-constant velocity

The axisymmetric non-uniform surface is assumed to move at a time-dependent velocity of $v_0(t) = a \times t = 10t$ μm/s at $r = 0$ mm, where $a = 10$ μm/s^2 is a constant acceleration. Fig. 8(a) shows the time-domain signal for $\Omega = -10\pi$ rad/s, which is a multi-component linear chirp as indicated by both the oscillating envelope and the gradually increasing frequency. The time-frequency representation using multisynchrosqueezing-based high-resolution time-frequency analysis [35] is shown in Fig. 8(b). The time-frequency representation has a strong energy before 0.1 s because of the sharp contrast in the time-domain signal. However, it is difficult to discriminate the multiple frequency components since they are so close, as shown in the upper-right inset in Fig. 8(b). After around 0.1 s, although the multiple frequency components separate gradually, the contrast of the time-domain signal decreases so that some of the frequency components are absent in the time-frequency representation. A compromise is to reduce the radial order of the LG beam from $p = 10$ to, for instance, $p = 5$ to enlarge the space between the adjacent frequency components, as shown in Fig. 8(c). The multiple frequency components are observed more clearly from 0.1 s to 0.3 s. In this period the best fits to the time-frequency ridges can be used to retrieve the multiple frequencies. Accordingly, the dynamic surface displacement at each radius r_n is obtained by $u_z(r_n)\big|_{t=t_0} = \int_0^{t_0} v(r_n, t)\,\mathrm{d}t = \int_0^{t_0} \lambda \cdot f_D(r_n, t)/2\,\mathrm{d}t$.

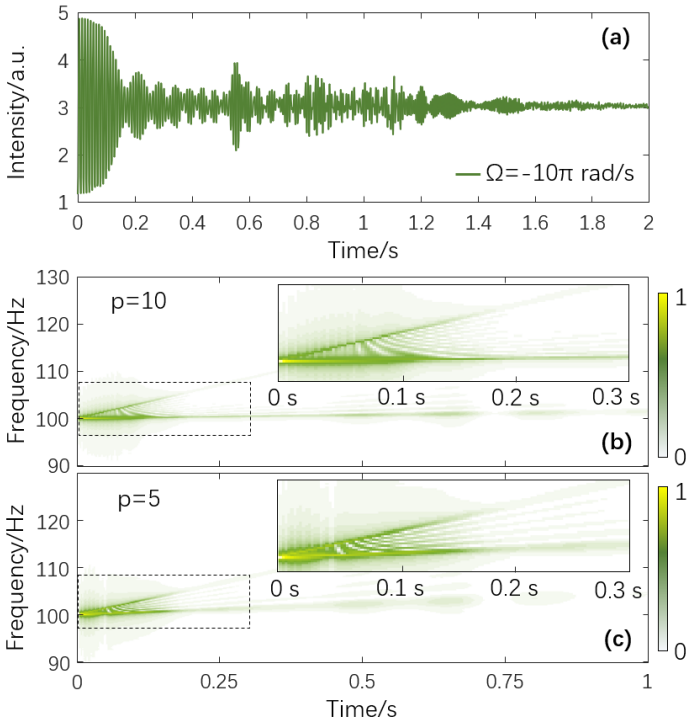

Fig. 8. (a) The time-domain signal for the axisymmetric non-uniform surface displacement with $v_0(t) = a \times t = 10t$ μm/s at $r = 0$ mm, $\Omega = -10\pi$ rad/s, and the radial order of the LG beam of $p = 10$. Only the signals within 2 s are displayed for visual clarity. (b) The time-frequency representation of the time-domain signal in (a). (c) The time-frequency representation of the time-domain signal for $p = 5$. The time-domain

signal is not displayed here. In (b) and (c), the upper-right insets zoom in on the dashed boxes; the colorbars on the right indicate the normalized energy of the time-frequency representations. Other parameters are $\ell = 10$ and $F_s = 400$ Hz.

We also investigated the time-domain signal for $v_0(t) = a(t) \times t$ at $r = 0$ mm, where $a(t)$ is a non-constant acceleration. A high-resolution time-frequency representation of such a multi-component quadratic chirp was not successful when this paper was written, which was limited by the narrow space between the frequency components at the beginning of the time-domain signal and the absence of frequency components due to the rapid decrease in the contrast of the time-domain signal. Therefore, the development of advanced time-frequency analysis techniques in future work is of great significance in dealing with such weak time-domain signals with a high-frequency resolution. Nonetheless, the basic measurement principle of the proposed COVI still holds.

6. DISCUSSIONS

6.1. Tilted surface displacement

Tilted surface displacement introduces an angle between the optical axis of the LG beam and the direction of the surface displacement velocity. We first investigated the effect of tilt angle on the carrier frequency. Figs. 9(a) – 9(e) show the carriers for the tilt angles of 0°, 0.01°, 0.02°, 0.05°, and 0.1°, respectively. The contrast of the carrier reduces significantly as the tilt angle increases. The frequency spectra of the carriers are shown in Figs. 9(f) – 9(j). The carrier frequency can be observed at 100 Hz for the different tilt angles, although the amplitude of the carrier frequency varies as the tilt angle increases. For the tilt angle larger than 0.02° a harmonic appears at 50 Hz. The harmonic is strongest for the tilt angle of 0.05°, which can be also observed in the carrier shown in Fig. 9(d). The reduction in the carrier contrast and the presence of the harmonic are attributed to the appearance of the moiré fringes [36] in the petal-like fringe pattern caused by the lateral shearing interference between the measurement LG beam and the reference LG beam, as illustrated in Fig. 9(k), where the fringe contrast decreases and the order of interference distorts.

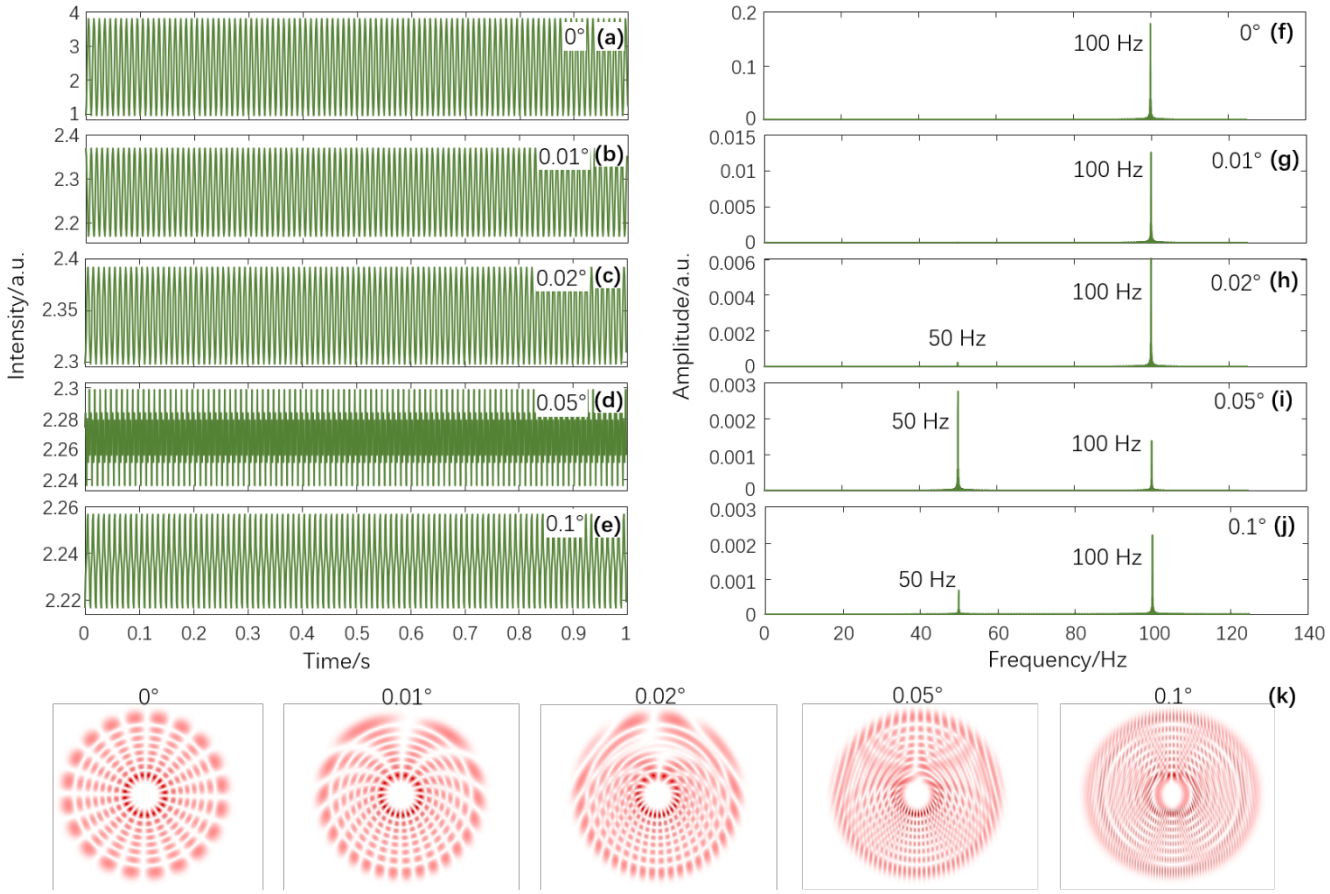

Fig. 9. (a) – (e) The carriers for the tilt angles of 0°, 0.01°, 0.02°, 0.05°, and 0.1°. (f) – (j) The frequency spectra of the carriers in (a) – (e), respectively. (k) The fringe patterns at $t = 1$ s before chopping for the tilt angles of 0°, 0.01°, 0.02°, 0.05°, and 0.1°. Note the difference in the vertical axis scale in (a) – (j). Other parameters are $\ell = 10$, $p = 7$, $\Omega = -10\pi$ rad/s, $\varphi_{SD} = 0$, and $F_s = 400$ Hz.

The effect of tilt angle on the measurement of uniform surface displacement at a constant velocity was then investigated. Fig. 10 shows the time-domain signals and the corresponding frequency spectra for the different tilt angles when $v_0 = 0.5$ μm/s, for instance. Since the unwanted moiré fringes appear in the fringe pattern as the tilt angle increases, as shown in Fig. 9(k), the time-domain signal for a large tilt angle results from chopping the rotating moiré fringe pattern instead of the rotating petal-like fringe pattern, causing the time-domain signals to vary in a complex manner. The Doppler frequency shift of 1.58 Hz to the right of the carrier frequency of 100 Hz can be observed because the fringe pattern and the chopper rotate in opposite directions. A harmonic appears at 1.58 Hz when the tilt angle reaches 0.01°. The harmonics around 50 Hz are shown as the tilt angle increases to 0.05°, which is consistent with Fig. 9(i), where a harmonic of the carrier frequency appears at 50 Hz when the tilt angle reaches 0.05°. In addition, the amplitude of the Doppler frequency shift to the right of the carrier frequency decreases and the one to the left of the carrier frequency increases as the tilt angle increases. This is attributed to that the moiré fringes become dominant in the fringe pattern when the tilt angle is larger than 0.05° and the moiré fringe pattern rotates in the

same direction as the chopping direction when the surface moves. We confirmed this by converting the angular velocity of the chopper from $\Omega = -10\pi$ rad/s to $\Omega = 10\pi$ rad/s. The time-domain signal and its frequency spectrum for the tilt angle of 0.1° are shown in Figs. 10(k) and 10(l). The Doppler frequency shift now switches back to the right of the carrier frequency.

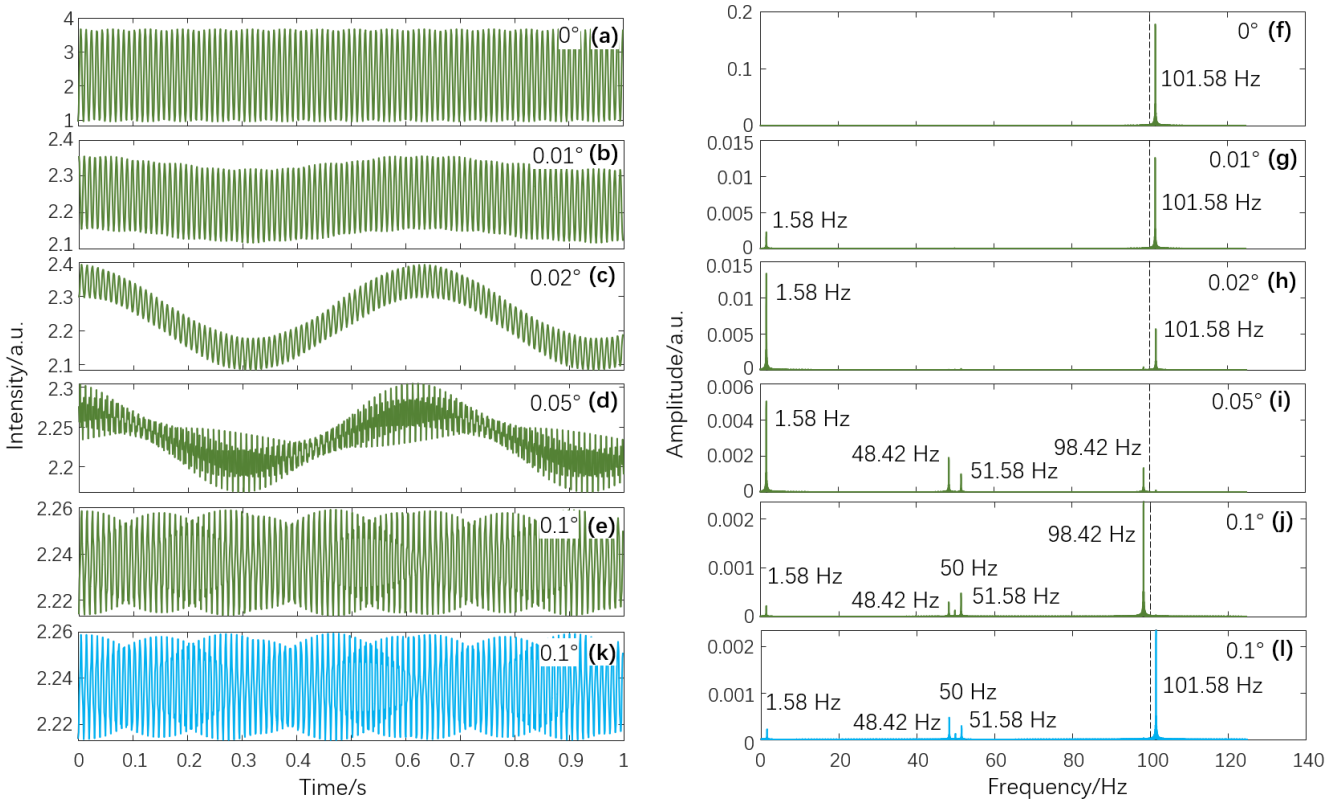

Fig. 10. (a) – (e) The time-domain signals for the uniform surface displacement with $v_0 = 0.5$ μm/s and the tilt angles of 0°, 0.01°, 0.02°, 0.05°, and 0.1° for $\Omega = -10\pi$ rad/s. (f) – (j) The frequency spectra of the time-domain signals in (a) – (e), respectively. The dashed line at 100 Hz indicates the carrier frequency. (k) and (l) are the time-domain signal and its frequency spectrum for the tilt angle of 0.1° and $\Omega = 10\pi$ rad/s. Note the difference in the vertical axis scale in (a) – (l). Other parameters are $\ell = 10$, $p = 7$, and $F_s = 400$ Hz.

Figure 11 shows the time-domain signals and their time-frequency representations for the uniform surface displacement at a time-dependent velocity of $v(t) = a \times t = 5t$ μm/s, for the different tilt angles. The characteristics of the Doppler frequency shift are identical to those in Fig. 10. Specifically, a linear up-chirp that starts at the carrier frequency of 100 Hz is shown. As the tilt angle increases, the energy of the linear up-chirp decreases and a harmonic with a frequency of 100 Hz less than the linear up-chirp appears. When the tilt angle increases from 0.02° to 0.1°, the linear up-chirp becomes weaker and a linear down-chirp that starts at the carrier frequency of 100 Hz becomes dominant, which is consistent with Figs. 10(h) – 10(j). The time-frequency representations for $v(t) = a(t) \times t$ are identical to Fig. 11 except that the linear chirps are replaced by the quadratic chirps.

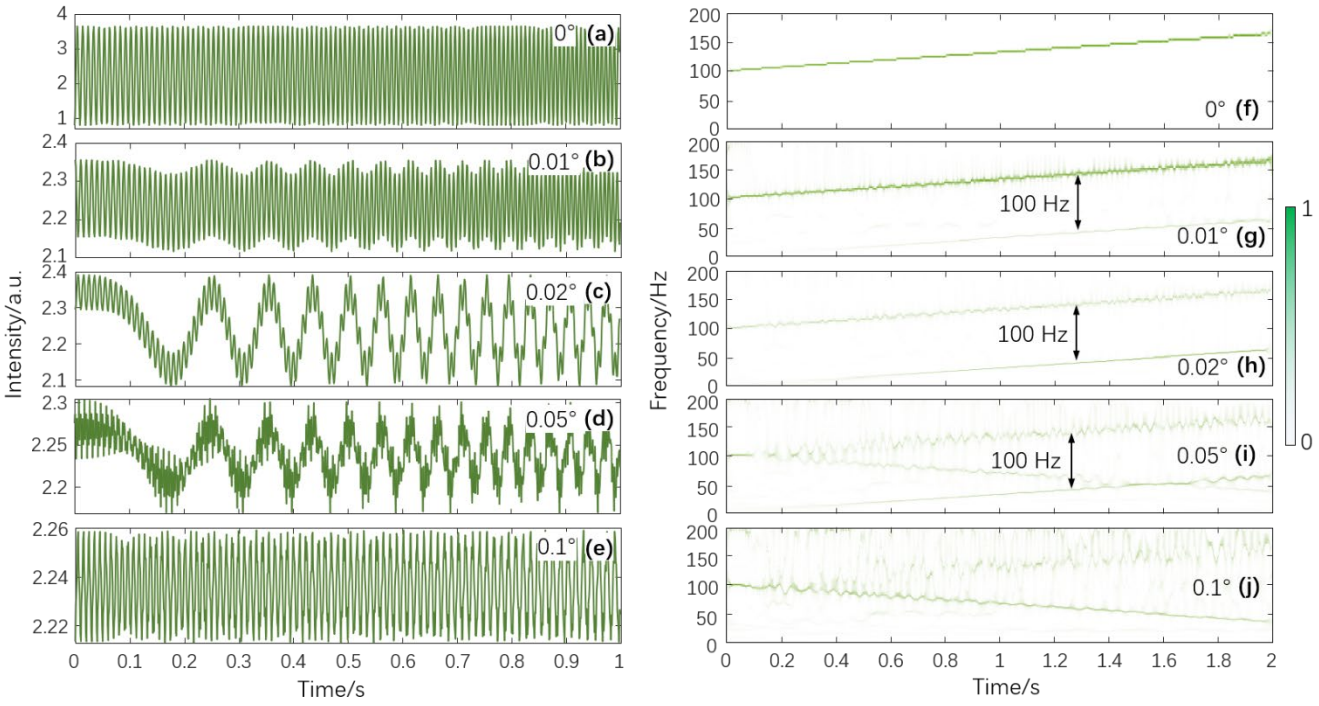

Fig. 11. (a) – (e) The time-domain signals for the uniform surface displacement with $v(t) = a \times t = 5t$ μm/s and the tilt angles of 0°, 0.01°, 0.02°, 0.05°, and 0.1°. (f) – (j) The time-frequency representations of the time-domain signals in (a) – (e), respectively. The colorbar on the right indicates the normalized energy of the time-frequency representations. Note the difference in the vertical axis scale in (a) – (e). Other parameters are $\ell = 10$, $p = 7$, $\Omega = -10\pi$ rad/s, and $F_s = 400$ Hz.

The effect of tilt angle on the measurement of axisymmetric non-uniform surface displacement at a constant velocity is shown in Fig. 12, which displays the time-domain signals and their frequency spectra for the different tilt angles when $v_0 = 1$ μm/s at $r = 0$ mm. Similarly, the variation among the time-domain signals is attributed to the moiré fringes induced at a large tilt angle, as illustrated in Fig. 12(k). Referring to Fig. 5, the tilted surface displacement results in different velocities at the same radius of the LG beam. In other words, as the bandwidth of the velocity broadens, so does that of the Doppler frequency. Therefore, as the tilt angle increases the Doppler frequency peaks become less pronounced than those in Fig. 12(f). Accordingly, the accuracy in locating the Doppler frequency peaks decreases. The Doppler peak frequencies calculated from the theoretical velocities at the radii r_n shown in Fig. 5 are taken as the theoretical ones, i.e., $f_D^{thr}(r_n) = 2v^{thr}(r_n)/\lambda$, and those estimated in Figs. 12(f) – 12(j) are taken as the ones retrieved numerically, i.e., $f_D^{rtr}(r_n)$. The frequency differences given by $f_D^{thr}(r_n) - f_D^{rtr}(r_n)$ are shown in the insets of Figs. 12(f) – 12(j), which confirm the accuracy degradation in locating the Doppler frequency peaks as the tilt angle increases.

If the non-uniform surface moves at a time-dependent velocity of $v_0(t) = a \times t$ or $v_0(t) = a(t) \times t$ at $r = 0$ mm, referring to both Fig. 8 and Fig. 12, it is straightforward to infer that the multiple frequency components in the linear chirp or the quadratic chirp will be aliased as the tilt angle increases.

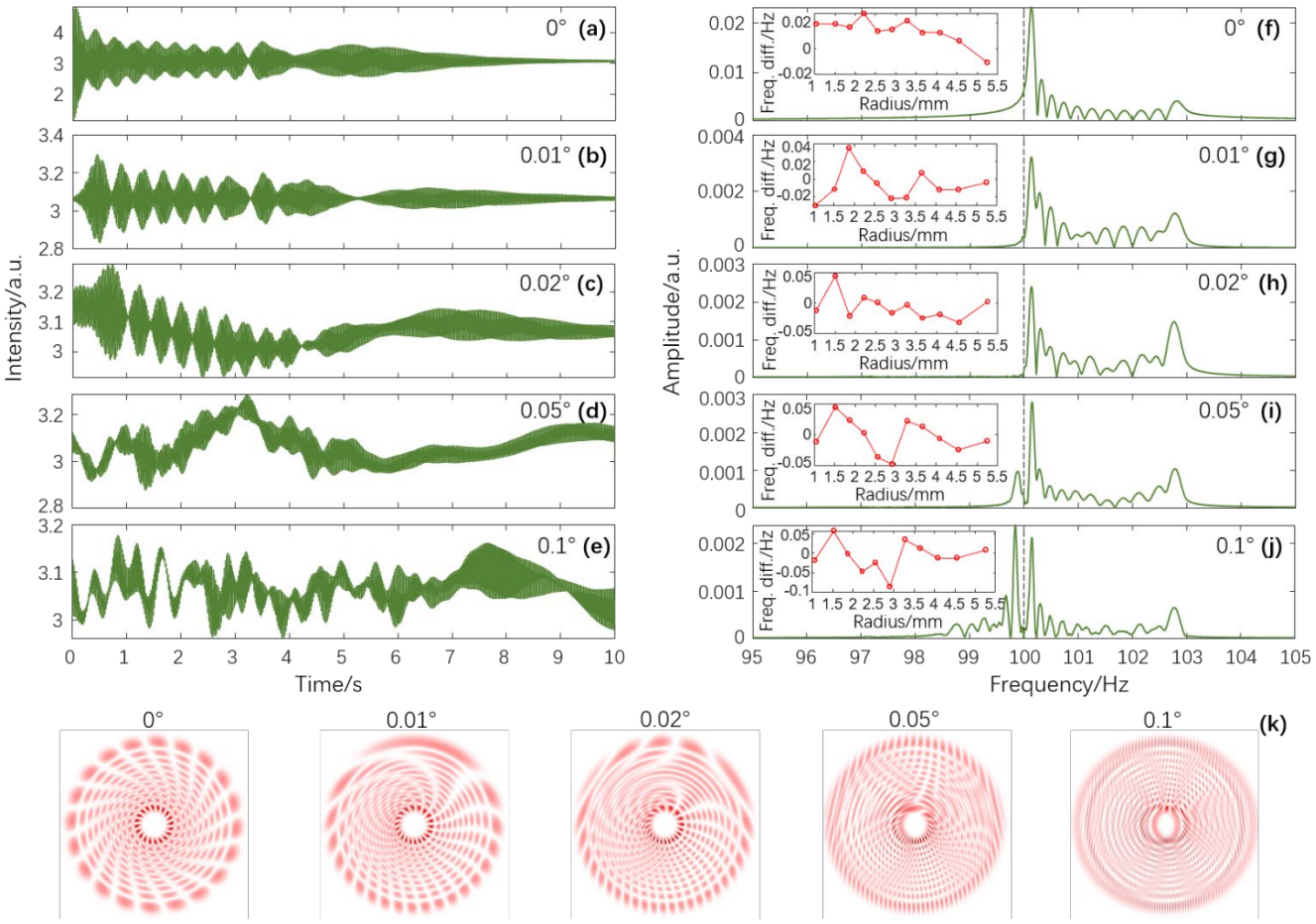

Fig. 12. (a) – (e) The time-domain signals for the non-uniform but axisymmetric surface displacement with $v_0 = 1$ μm/s at $r = 0$ mm and the tilt angles of 0°, 0.01°, 0.02°, 0.05°, and 0.1°. (f) – (j) The frequency spectra of the time-domain signals in (a) – (e), respectively. The dashed line at 100 Hz indicates the carrier frequency. The insets are the differences between the theoretical and retrieved Doppler peak frequencies at the radii r_n. (k) The fringe patterns at $t = 1$ s before chopping for the tilt angles of 0°, 0.01°, 0.02°, 0.05°, and 0.1°. Note the difference in the vertical axis scale in (a) – (j) and the insets. Other parameters are $\ell = 10$, $p = 10$, $\Omega = -10\pi$ rad/s, and $F_s = 250$ Hz.

6.2. Lateral offset of the surface displacement

The lateral offset refers to the distance between the centre of the LG beam and the centre of the surface deformation. The lateral offset has no effect on the uniform surface displacement. The effect of lateral offset on the measurement of the axisymmetric non-uniform surface displacement is shown in Fig. 13, where the surface moves at $v_0 = 1$ μm/s at $r = 0$ mm and the lateral offsets are 0, 0.05, 0.1, 0.2, and 0.5 mm. As the lateral offset increases, the measurement wavefront reflected from

the offset surface becomes non-axisymmetric, so the periodicity of the fringe pattern in the azimuthal direction is broken, as shown in Fig. 13(k). The non-periodicity results in the weakened oscillating behaviour of the time-domain signal while the fringe pattern is chopped. Moreover, referring to Fig. 5, the lateral offset leads to the broadened frequency bandwidth because of the broadened velocity bandwidth at the same radii of the LG beam. Therefore, the Doppler frequency peaks overlap each other, and eventually cannot be distinguished. The insets in Figs. 12(f) – 12(j) show the differences between the theoretical and numerically retrieved Doppler peak frequencies at the radii r_n. The lateral offset degrades the accuracy in locating the Doppler frequency peaks. This result is applicable to the non-uniform surface moving at a non-constant velocity as well.

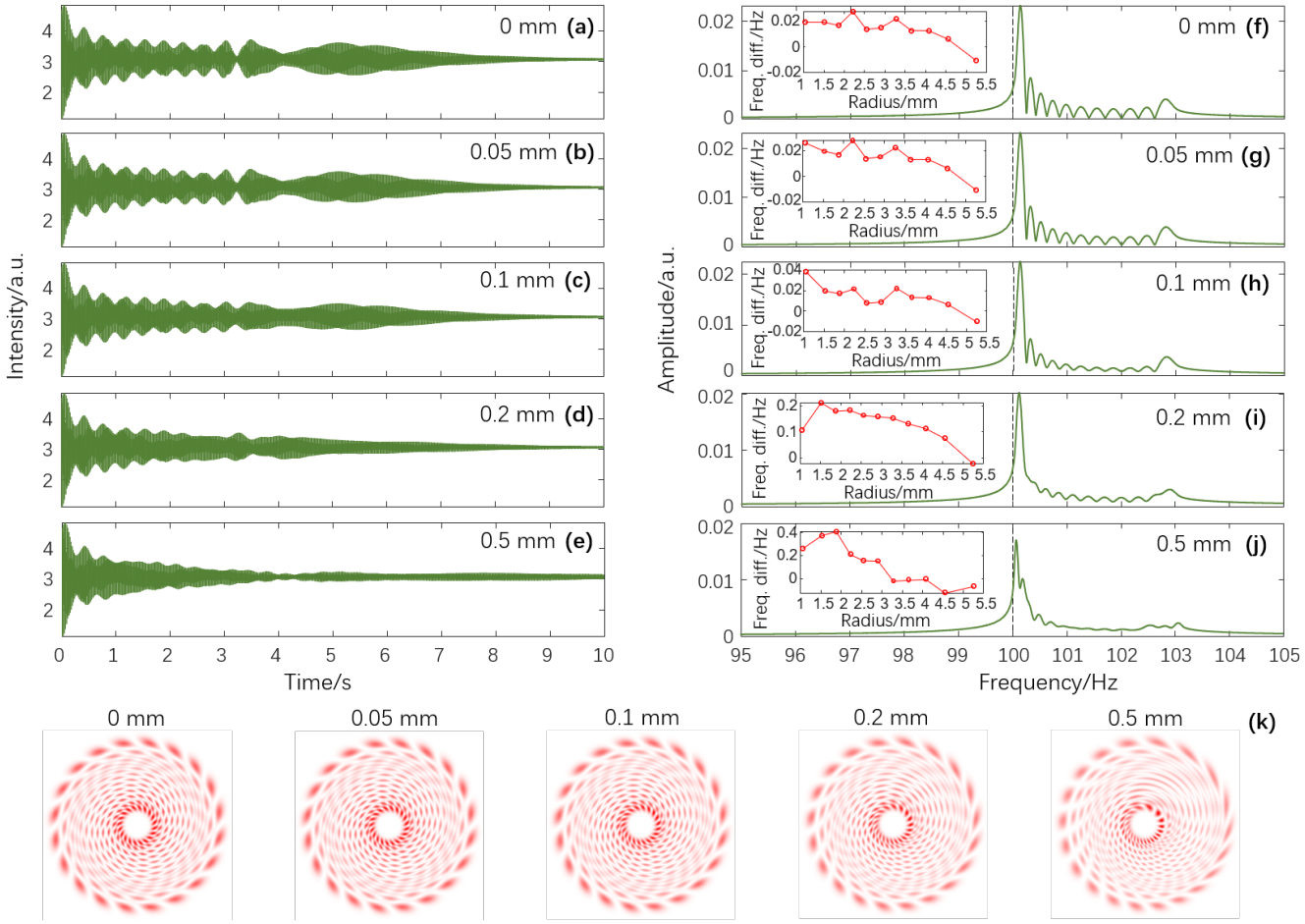

Fig. 13. (a) – (e) The time-domain signals for the axisymmetric non-uniform surface displacement with v_0 = 1 μm/s at r = 0 mm and the lateral offsets of 0, 0.05, 0.1, 0.2, and 0.5 mm. (f) – (j) The frequency spectra of the time-domain signals in (a) – (e), respectively. The dashed line at 100 Hz indicates the carrier frequency. The insets are the differences between the theoretical and retrieved Doppler peak frequencies at the radii r_n. (k) The fringe patterns at t = 3 s before chopping for the lateral offsets of 0, 0.05, 0.1, 0.2, and 0.5 mm. Other parameters are ℓ = 10, p = 10, Ω = –10π rad/s, and F_s = 250 Hz.

6.3. Limiting factors of the measurable velocity

In the proposed COVI, the measurement of dynamic surface displacement is obtained by the measurement of the surface displacement velocity via retrieving the Doppler frequency shift. The upper and lower limits of the measurable velocity for the scenarios of uniform and non-uniform surface displacement are different and should be discussed separately.

Scenario 1: The upper limit of the velocity for the uniform surface displacement is determined by the carrier frequency f_c referring to Figs. 3(c), 4(c) and 4(d). The Doppler frequency shift f_D is typically limited in the range of $(0, f_c)$. Smaller carrier frequency results in a lower upper limit of the velocity. One can reverse the chopping direction to circumvent this problem, so that f_D is within the range of (f_c, ∞). In this case, a band-pass filter with a bandwidth of B and a central frequency of $f_c+B/2$ can be applied in the COVI to eliminate the high-frequency noise and the DC drift. The upper limit of the velocity is therefore given by $(f_c+B)\lambda/2$. For instance, one can choose f_c = 100 Hz and B = 100 Hz, allowing the COVI working at a high frequency of $f_c+B/2$ = 150 Hz. Thus, the upper limit of the velocity is $(f_c+B)\lambda/2$ = 47.475 μm/s.

The lower limit of the velocity can infinitely approach zero in theory as long as the accuracy in estimating f_D is infinitely high. This accuracy is limited by both the noise floor and the DFT bin. The noise floor can be minimised by using a stabilised laser, low noise circuits and keeping the interferometer away from disturbance. The DFT bin, having a width determined by the frequency resolution of $\Delta f = F_s/N$, should match the exact value of $f_c + f_D$, i.e., $(f_c + f_D)/\Delta f = Q$ with Q being an integer other than one. The above equation can help determine F_s and N in practice. For instance, if one would like to determine the velocity of as low as v_0 = 30 nm/s, which corresponds to $f_D = 2v_0/\lambda$ = 0.095 Hz, then it should be satisfied that $\Delta f \times Q = F_s/N \times Q = f_c + f_D$ = 100.095 Hz. Suppose that the sampling rate is F_s = 500 Hz, then Q/N = 0.20019 with Q and N being both integers. One can simply choose Q = 20019 and $N = 10^4$.

Scenario 2: The upper limit of the velocity for the non-uniform surface displacement is determined by its dynamic range besides the carrier frequency or the bandwidth of the band-pass filter discussed previously. The dynamic range is given by the effective length of the time-domain signal that starts from t = 0 s and ends at where the oscillation vanishes, as shown in Figs. 6(a) and 8(a). This is because the highly twisted and stretched petal-like fringes subjected to a large non-uniform surface displacement lose the periodicity in the azimuthal direction, as shown in the insets of Fig. 6(a), so that the total intensity of the chopped fringe pattern changes inconsiderably. Therefore, larger velocity of the non-uniform surface displacement results in a shorter sampling length of the time-domain signal and a larger error of frequency and velocity estimation. For instance, if the upper limit of the velocity is 5 μm/s, the oscillation of the time-domain signal will vanish at around t = 2 s. Given by F_s = 250 Hz, then the sampling length is only N = 500, resulting in a frequency resolution of $\Delta f = F_s/N$ = 0.2 Hz only and accordingly a velocity error of $\Delta v = \Delta f \times \lambda/2$ = 63.3 nm/s. In contrast, the upper limit of the velocity of 0.5 μm/s results in t = 20 s, N = 5000, $\Delta f = F_s/N$ = 0.02 Hz and $\Delta v = \Delta f \times \lambda/2$ = 6.33 nm/s.

The factors affecting the lower limit of the velocity are basically the same as those in Scenario 1 except that p+1 Doppler peak frequencies corresponding to the radii of the rings of the LG beam should fall right into DFT bins simultaneously, i.e., $[f_c + f_D(r_n)]/\Delta f = Q_n$ with Q_n being p+1 integers other than one. Apparently, the above equation is more restrictive than that in Scenario 1. For instance, if one would like to determine the velocities of $v(r_1) = 60$ nm/s, $v(r_2) = 50$ nm/s, $v(r_3) = 40$ nm/s, and $v(r_4) = 30$ nm/s, which correspond to $f_D(r_1) = 0.19$ Hz, $f_D(r_2) = 0.158$ Hz, $f_D(r_3) = 0.126$ Hz, and $f_D(r_4) = 0.095$ Hz, respectively, then it should be satisfied that $\Delta f \times Q_1 = F_s/N \times Q_1 = 100.19$ Hz, $\Delta f \times Q_2 = F_s/N \times Q_2 = 100.158$ Hz, $\Delta f \times Q_3 = F_s/N \times Q_3 = 100.126$ Hz, and $\Delta f \times Q_4 = F_s/N \times Q_4 = 100.095$ Hz, respectively. Suppose $F_s = 500$ Hz, then we have $Q_1/N = 0.20038$, $Q_2/N = 0.200316$, $Q_3/N = 0.200252$, and $Q_4/N = 0.20019$ with Q_1, Q_2, Q_3, Q_4, and N being all integers. One can simply choose $Q_1 = 100190$, $Q_2 = 100158$, $Q_3 = 100126$, $Q_4 = 100095$ and $N = 5\times10^5$. Therefore, the sampling length N will become considerably large to satisfy that Q_n are all integers. Alternatively, the advanced frequency estimation algorithms [37-39] can be applied to approximate the exact value of $f_D(r_n)$ if $f_D(r_n)$ doesn't fall right into a DFT bin.

7. CONCLUSIONS

We put forward a COVI with a novel method of fringe pattern demodulation based on Doppler frequency shift for the dynamic surface displacement measurement at nanometre to micrometre-scale. The advantages of the COVI are summarised in two aspects. One aspect is that the deployment of the chopper and the point photodetector converts 2D fringe patterns into a 1D time-domain signal, which consequently overcomes the shortcomings of the conventional pixelated morphological operations. The time-domain signal is referred to as the carrier in the absence of surface displacement. A Doppler frequency shift is introduced with respect to the carrier frequency in the presence of dynamic surface displacement. The other one is that the employment of a p-radial order LG beam that exhibits p+1 concentric rings fills the gap of the axisymmetric non-uniform surface displacement measurement using optical vortex interferometers. Each ring with a specific radius carries a specific surface displacement velocity, causing the Doppler frequency shift to split into p+1 peaks. Locating the Doppler frequency peaks gives the velocities at those radii. The dynamic surface displacement at those radii can then be obtained by integrating the velocities over time.

We described the basic working principle of the COVI in rigorous mathematics and verified it numerically in the scenarios of uniform and axisymmetric non-uniform surface displacement measurements. Compared with the previous work [30], the new findings are concluded as follows. *i*) The Doppler frequency shift can be accurately retrieved using either the DFT for the constant surface displacement velocity or the time-frequency analysis for the non-constant velocity. *ii*) For the constant surface displacement velocity, we pointed out that the relative error of ±3% between the theoretical Doppler peak frequencies and the retrieved ones is attributed to the DFT bin and the discretisation error. The former can be alleviated by improving the frequency

resolution. The latter is valid in the numerical calculation only and can be minimised in the experiment. *iii*) For the non-constant surface displacement velocity, the maximum energy ridge can be extracted from the time-frequency representation to obtain the time-dependent Doppler frequency shift. We also admitted that high-resolution time-frequency analysis techniques are vital to study the multi-component non-stationary signal in the COVI. *iv*) Surface misalignment including tilt and lateral offset introduces harmonics of Doppler frequency shift and causes frequency aliasing in Doppler frequency splitting. Specifically, we verified that the Doppler frequency shifts can be estimated correctly for tilt angles less than 0.05° and lateral offsets less than 0.1 mm. For tilt angles larger than 0.05° and lateral offset larger than 0.1 mm, the main error in locating the Doppler frequency peaks results from the frequency bandwidth broadening due to the broadened velocity bandwidth at the radius of each ring of the LG beam. *v*) The factors affecting the upper limit of the measurable displacement velocity were discussed to be the carrier frequency, the bandwidth of the band-pass filter and the dynamic range of the displacement measurement. The lower limit of the velocity is affected by the noise floor and the DFT bin as well as the frequency resolution. We also gave instructions on the determination of the DFT bin for accurate frequency estimation in practice. The proposed COVI paves the way for expanding the application field of optical vortex interferometers and the results of the work provide a comprehensive understanding of how to measure a dynamic surface displacement using the COVI.

ACKNOWLEDGMENTS

We acknowledge the National Natural Science Foundation of China (Grant No. 52275528), Hefei Municipal Natural Science Foundation (Grant No.2022018), China Scholarship Council (Grant No. 202206695004), European Union's Horizon 2020 Research and Innovation Programme (DAT4.ZERO, 958363), and UKRI Research England Development (RED) Fund via the Midlands Centre for Data-Drive Metrology.

DECLARATION OF COMPETING INTEREST

The authors declare that they have no known competing financial interests or personal relationships that could have appeared to influence the work reported in this paper.

DATA AVAILABILITY

The data that support the findings of this study are available from the corresponding author upon reasonable request.

REFERENCES

1. X. Li, Y. Zhao, T. Hu, and Y. Bai, "Design of a high-speed electrothermal linear micromotor for microelectromechanical systems safety-and-arming devices," Micro & Nano Letters **11**, 692-696 (2016).

2. Y. X. He, R. J. Li, J. Li, W. K. Zhao, Z. Y. Cheng, Q. X. Huang, and K. C. Fan, "Novel Compensation Method of Volumetric Errors for Micro-Coordinate Measuring Machines Using Abbe and Bryan Principles," IEEE Transactions on Instrumentation and Measurement **71**, 1-10 (2022).
3. E. Manske, "Nanopositioning and Nanomeasuring Machines," in *Metrology*, W. Gao, ed. (Springer Singapore, Singapore, 2019), pp. 35-58.
4. E. Manske, T. Fröhlich, R. Füßl, I. Ortlepp, R. Mastylo, U. Blumröder, D. Dontsov, M. Kühnel, and P. Köchert, "Progress of nanopositioning and nanomeasuring machines for cross-scale measurement with sub-nanometre precision," Measurement Science and Technology **31**, 085005 (2020).
5. G. Jäger, E. Manske, T. Hausotte, A. Müller, and F. Balzer, "Nanopositioning and nanomeasuring machine NPMM-200—a new powerful tool for large-range micro- and nanotechnology," Surface Topography: Metrology and Properties **4**, 034004 (2016).
6. U. Blumröder, P. Köchert, J. Flügge, R. Füßl, I. Ortlepp, and E. Manske, "Comb-referenced metrology laser for interferometric length measurements in nanopositioning and nanomeasuring machines," **89**, 687-703 (2022).
7. O. A. Capeloto, V. S. Zanuto, G. V. B. Lukasievicz, L. C. Malacarne, S. E. Bialkowski, T. Požar, and N. G. C. Astrath, "Generation and detection of thermoelastic waves in metals by a photothermal mirror method," Applied Physics Letters **109**, 191908 (2016).
8. G. A. S. Flizikowski, B. Anghinoni, J. H. Rohling, M. P. Belançon, R. S. Mendes, M. L. Baesso, L. C. Malacarne, T. Požar, S. E. Bialkowski, and N. G. C. Astrath, "Influence of edge effects on laser-induced surface displacement of opaque materials by photothermal interferometry," Journal of Applied Physics **128**, 044509 (2020).
9. G. Verma, G. Yadav, C. S. Saraj, L. Li, N. Miljkovic, J. P. Delville, and W. Li, "A versatile interferometric technique for probing the thermophysical properties of complex fluids," Light: Science & Applications **11**, 115 (2022).
10. J. N. Reddy, *Theory and analysis of elastic plates and shells* (CRC press, 2006).
11. G. Verma and G. Yadav, "Compact picometer-scale interferometer using twisted light," Optics Letters **44**, 3594-3597 (2019).
12. S. Bialkowski, N. Astrath, and M. Proskurnin, *Photothermal Spectroscopy Methods, Second Edition* (John Wiley & Sons, Inc. , 2019).
13. O. Emile and J. Emile, "Naked eye picometer resolution in a Michelson interferometer using conjugated twisted beams," Optics Letters **42**, 354-357 (2017).
14. Q. Jia, X. Qiu, Z. Wu, W. Zhang, and L. Chen, "Transferring linear motion of an optical wedge to rotational frequency shift in an orbital angular momentum interferometer," Applied Physics Letters **111**, 091102 (2017).
15. A. Serrano-Trujillo and M. E. Anderson, "Surface profilometry using vortex beams generated with a spatial light modulator," Optics Communications **427**, 557-562 (2018).
16. H. Lu, Y. Hao, C. Guo, X. Huang, H. Hao, D. Guo, H. Zhao, W. Tang, P. Wang, and H. Li, "Nano-Displacement Measurement System Using a Modified Orbital Angular Momentum Interferometer," IEEE Journal of Quantum Electronics **58**, 7500105 (2022).
17. P. Munjal, K. Chaudhary, and K. P. Singh, "Noise self-canceling picoscale twisted interferometer," Optics Letters **47**, 5993-5996 (2022).
18. J. Zhu, L. Wang, J. Ji, and S. Zhao, "Real-time measurement of dynamic micro-displacement and direction using light's orbital angular momentum," Applied Physics Letters **120**, 251104 (2022).
19. D. Zhao, C. Jia, Y. Ma, X. Yang, B. Zhang, and W. Chu, "High-Accuracy Surface Profile Measurement Based on the Vortex Phase-Shifting Interferometry," International Journal of Optics **2021**, 6937072 (2021).
20. L. Zhang, J. Cao, S. Wu, R. Liu, J. Wu, and B. Yu, "From concept to reality: computing visual vortex beam interferometer for displacement measurement," Optics Letters **47**, 5449-5452 (2022).
21. Y. Ding, T. Liu, S. Qiu, Z. Liu, Q. Sha, and Y. Ren, "Locating the center of rotation of a planar object using an optical vortex," Applied Optics **61**, 3919-3923 (2022).
22. Y. Ma, F. Yang, and D. e. Zhao, "Calibration of the Soleil-Babinet Compensator Based on the Vectorial Optical Field," Photonics **9**, 416 (2022).
23. N. M. Kerschbaumer, L. I. Fochler, M. Reichenspurner, S. Rieger, M. Fedoruk, J. Feldmann, and T. Lohmüller, "Twisted light Michelson interferometer for high precision refractive index measurements," Optics Express **30**, 29722-29734 (2022).
24. Z.-Y. Zhou, Y. Li, D.-S. Ding, W. Zhang, S. Shi, and B.-S. Shi, "Optical vortex beam based optical fan for high-precision optical measurements and optical switching," Optics Letters **39**, 5098-5101 (2014).
25. A. Jesacher, S. Fürhapter, S. Bernet, and M. Ritsch-Marte, "Spiral interferogram analysis," J. Opt. Soc. Am. A **23**, 1400-1409 (2006).
26. A. L. Vadnjal, P. Etchepareborda, A. Bianchetti, F. E. Veiras, A. Federico, and G. H. Kaufmann, "Comparison of phase recovery methods in spiral speckle pattern interferometry correlation fringes," Optics and Lasers in Engineering **80**, 63-72 (2016).
27. M. Xiao, D. Yang, and J. Xiong, "Non-contact measurement for cone angle of axicon lens based on vortex interference," Optics Communications **499**, 127267 (2021).

28. D. Yang, Z. Yang, Z. Zhao, and Z. Liu, "Radius of curvature of spherical wave measurement based on vortex beam interference," Optics and Lasers in Engineering **142**, 106592 (2021).
29. J. Zeng, Y. Dong, Y. Wang, J. Zhang, and J. Wang, "Optical Imaging using Orbital Angular Momentum: Interferometry, Holography and Microscopy," Journal of Lightwave Technology **41**, 1-18 (2022).
30. J. Dong, Z. Tian, S. Wang, L. Xie, Y. Li, and E. Zhao, "Dynamic non-uniform phase shift measurement via Doppler frequency shift in vortex interferometer," Optics Letters **48**, 2018-2021 (2023).
31. E. Bolduc, N. Bent, E. Santamato, E. Karimi, and R. W. Boyd, "Exact solution to simultaneous intensity and phase encryption with a single phase-only hologram," Optics Letters **38**, 3546-3549 (2013).
32. G. Huang, D. Wu, J. Luo, L. Lu, F. Li, Y. Shen, and Z. Li, "Generalizing the Gerchberg-Saxton algorithm for retrieving complex optical transmission matrices," Photon. Res. **9**, 34-42 (2021).
33. I. The MathWorks, "Amplitude Estimation and Zero Padding", retrieved 8 March, 2023, https://uk.mathworks.com/help/signal/ug/amplitude-estimation-and-zero-padding.html.
34. G. Thakur, E. Brevdo, N. S. Fučkar, and H.-T. J. S. P. Wu, "The synchrosqueezing algorithm for time-varying spectral analysis: Robustness properties and new paleoclimate applications," **93**, 1079-1094 (2013).
35. G. Yu, "A multisynchrosqueezing-based high-resolution time-frequency analysis tool for the analysis of non-stationary signals," Journal of Sound and Vibration **492**, 115813 (2021).
36. G. T. Reid, "Moiré fringes in metrology," Optics and Lasers in Engineering **5**, 63-93 (1984).
37. Ç. Candan, "Analysis and further improvement of fine resolution frequency estimation method from three DFT samples," IEEE Signal Processing Letters **20**, 913-916 (2013).
38. U. Orguner and Ç. Candan, "A fine-resolution frequency estimator using an arbitrary number of DFT coefficients," Signal processing **105**, 17-21 (2014).
39. K. Wang, H. Wen, and G. Li, "Accurate frequency estimation by using three-point interpolated discrete fourier transform based on rectangular window," IEEE Transactions on Industrial Informatics **17**, 73-81 (2020).